Special Issue: Aeroacoustics and non-linear structural dynamics in Turbomachines

Numerical investigation of noise reduction mechanisms in a bio-inspired airfoil

Andrew Bodling, Anupam Sharma *

Department of Aerospace Engineering Iowa State University, 2341 Howe Hall, Ames, IA, 50011, USA

ARTICLE INFO

ABSTRACT

This paper presents a numerical analysis of an airfoil geometry inspired by the down coat of the night owl. The objective is to understand the mechanisms of airfoil trailing edge noise reduction that has been observed with such designs in previous experiments. The bioinspired geometry consists of an array of finlet "fences" that are applied near the trailing edge of the baseline (NACA 0012) airfoil. Wall-resolved large eddy simulations are performed over the baseline and the bioinspired airfoil geometries and the aeroacoustic performance of the two geometries are contrasted. Both models are simulated at chord-based Reynolds number $Re_c = 5 \times 10^5$, flow Mach number, $M_\infty = 0.2$, and angle of attack, $\alpha = 0°$. Unsteady surface pressure spectra near the airfoil trailing edge show large reductions at high frequencies but an increase in low frequencies with the bioinspired airfoil, consistent with previous measurements. Farfield noise spectra comparisons between the baseline and the bioinspired airfoil show reductions of up to 10 dB with the fences. The simulations reveal that the fences lift the turbulence eddies away from the airfoil trailing (scattering) edge hence reducing the scattering efficiency. These findings suggest that one of the mechanisms of noise reduction is the increased source-scattering edge separation distance. Two-point correlations show that the fences reduce the spanwise coherence at low frequencies for separation distances greater than a fence pitch. Reduction in spanwise coherence is another potential mechanism of farfield noise reduction at low frequencies.

© 2019 Elsevier Ltd. All rights reserved.

1. Introduction

One biological feature that has yet to be used in engineering innovations is the silent flight of nocturnal owls. One species of nocturnal owls - the barn owl (Tyto alba) - is particularly adept at silent flight. In this paper, we refer to the barn owl as 'the owl'. The owl has unique feather features – the leading edge (LE) comb, the down coat on flight feathers, and the trailing edge (TE) fringes – which are collectively referred to as the "hush kit". There has been considerable research on using LE and TE features, modeled as serrations, to reduce airfoil noise [1–3]. The down coat has been investigated analytically [4,5] and experimentally [6,7]. However, little to no numerical research has been performed to investigate the acoustic impact of the owl down coat. This paper uses high-resolution large eddy simulations to perform diagnosis of sound sources in blade designs inspired by the down coat of owl feathers.

The particular bioinspired blade designs that form the focus of this paper were first discussed by Clark et al. [6]. They suggested that the down coat (made of hairs that rise up vertically and plateau in the flow direction) forms a canopy and makes

---

* Corresponding author.

E-mail address: sharma@iastate.edu (A. Sharma).
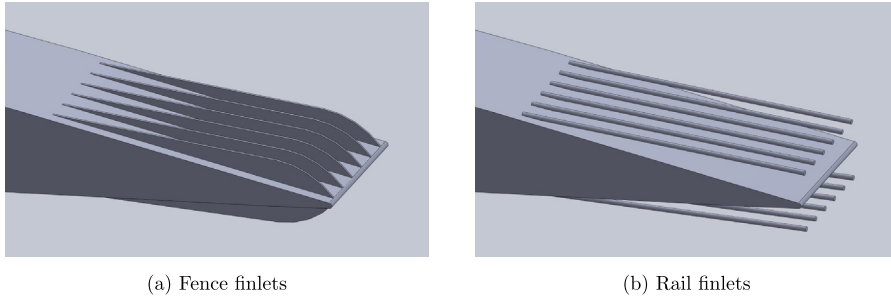
(a) Fence finlets   (b) Rail finlets

Fig. 1. Idealized schematics of the two finlet designs used by Clark et al. [7].

the flow behave similarly to forest canopy flows. They attempted to reproduce this canopy effect using "finlets" which were constructed in two different ways - (a) using an array of sharp edge fences, and (b) using tiny cylindrical rails. Clark et al. [6,7] presented aeroacoustics measurements of trailing edge noise from airfoils with these finlets (fences and rails) installed using a substrate near the trailing edge of the baseline airfoil. The DU96-W-180 airfoil, commonly used in wind turbine applications, was selected as the baseline in these experiments.

Fig. 1 shows the schematics of the two finlet designs used in the experiments [6,7]. Plots (a) and (b) in the figure are the fence and rail configurations, respectively. Farfield sound measurements made using acoustic beamforming [8] showed that the finlet designs were significantly quieter than the baseline airfoil [7].

This paper presents results of highly-resolved large eddy simulations of a baseline airfoil as well as the baseline airfoil fitted with two different designs of finlet fences. It should be noted that the baseline airfoil used in this study is NACA 0012 while the experiments of Ref. [7] used the DU96-W-180 airfoil. Also, the simulations are performed at a chord-based Reynolds number $Re_c^{(sim)} = 5 \times 10^5$, which is smaller than that of the experiments $Re_c^{(exp)} = 2.1 \times 10^6$. These simplifications are made to manage the complexity and the computational requirements to solve the problem. Nevertheless, the simulations reveal several interesting flow physics that shed new light on the potential mechanisms of the observed noise reduction, thus supplementing the experimental results of Ref. [7]. This research builds upon authors' previous studies in simulating finlet fences [9,10]. Bodling et al. [9,10] modeled the finlet fences as a single-step geometry by varying the height of the fences in a single discrete step (as opposed to a continuous variation in the experiment model). Although the single-step design was successful in reducing the unsteady surface pressure fluctuations on the airfoil surface near the airfoil trailing edge, it did not result in the farfield noise reduction observed in the experiments of Ref. [7]. In this article, we focus on the aeroacoustic impact of the geometry of the leading edge of the finlet fences. Results from three sets of simulations are presented and compared: (a) baseline airfoil (NACA 0012), and the baseline airfoil with finlet fences installed where the leading edge of the fence is modeled as a (b) single-step, and (c) as a stair-step. Fig. 2 contrasts the geometries of the fences used in the experiments with those used in the simulations.

In the experiments, the leading edge of the fence is nearly parallel to the flow while in the "single-step" geometry, the leading edge is orthogonal to the flow. Potential problems with the orthogonal leading edge in the single-step simulation include a) scattering of the boundary layer turbulence into radiated sound, and b) production of turbulence at the sharp edge. To alleviate this problem and to better match the experimental geometry, the fence is modeled using a "stair-step" geometry in this paper. While the simulated stair-step geometry is still an approximation to the smooth edge in the experiments, the smaller vertical jumps are de-correlated by spatial separation and hence not as efficient in acoustic scattering.

The objective is to make qualitative comparisons between the measurements and the predictions with the stair-step leading edge fence geometry to gain confidence in the simulations, and then perform source diagnostics using the highly-resolved flowfield to enhance understanding of the noise reduction mechanisms of finlets.

2. Numerical methodology

A two-step approach is used for farfield noise prediction. Fluid flow simulations are first carried out using a computational fluid dynamics (CFD) solver and subsequently, an integral method (acoustic analogy) is used with the CFD data to compute the radiated noise in the far-field. The compressible Navier-Stokes solver, FDL3DI [11] is used for the fluid flow simulations. The numerical approach used here has been previously validated by the authors and utilized to assess noise reduction ability of leading edge serrations [3,12]. Brief descriptions of the flow solver and the noise radiation solver are provided below for completeness.

The compressible Navier-Stokes solver, FDL3DI [11], is used for the fluid flow simulations. The governing fluid flow equations (solved by FDL3DI), after performing a time-invariant curvilinear coordinate transform $(x, y, z) \rightarrow (\xi, \eta, \zeta)$, are written in a strong conservation form as

$$\frac{\partial}{\partial t}\left(\frac{\mathbf{U}}{J}\right) + \frac{\partial \widehat{\mathbf{F}}_I}{\partial \xi} + \frac{\partial \widehat{\mathbf{G}}_I}{\partial \eta} + \frac{\partial \widehat{\mathbf{H}}_I}{\partial \zeta} = \frac{1}{Re}\left[\frac{\partial \widehat{\mathbf{F}}_\nu}{\partial \xi} + \frac{\partial \widehat{\mathbf{G}}_\nu}{\partial \eta} + \frac{\partial \widehat{\mathbf{H}}_\nu}{\partial \zeta}\right], \tag{1}$$

(a) Experiments

(b) Simulation - "single-step"
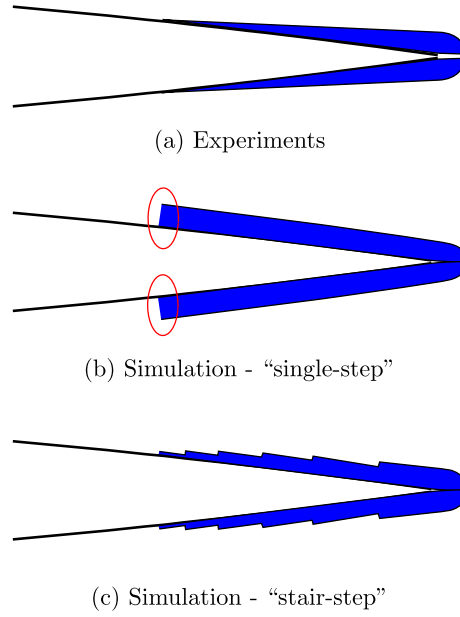
(c) Simulation - "stair-step"

Fig. 2. Schematics highlighting the differences in the fence geometries between the experiments and the current simulations.

where J is the Jacobian of the coordinate transformation, $\mathbf{U} = \{\rho, \rho u, \rho v, \rho w, \rho E\}$; the expressions for inviscid flux terms, $\widehat{\mathbf{F}}_I, \widehat{\mathbf{G}}_I, \widehat{\mathbf{H}}_I$ and viscous flux terms, $\widehat{\mathbf{F}}_v, \widehat{\mathbf{G}}_v, \widehat{\mathbf{H}}_v$ are provided in Ref. [11]. We perform 'implicit' LES (ILES) simulations using FDL3DI by employing sixth-order spatial accuracy, eighth-order low pass filters, and a second order, implicit time integration scheme.

Far-field sound propagation is performed using the Ffowcs Williams-Hawkings (FW-H) acoustic analogy [13]. For low-Mach number flows ($M \leq 0.2$) the volume sources are much weaker than the surface sources and can be neglected. Using this assumption, the following integral equation is obtained for far-field acoustic pressure, p' at location $\mathbf{x}$ and time t:

$$p'(\mathbf{x}, t) = \frac{1}{4\pi |1 - M_r| |\mathbf{x}|} \left(\frac{\partial}{\partial t} \iint [\rho_0 u_i n_i + \rho'(u_i - U_i) n_i] d\Sigma + \frac{x_i}{c |\mathbf{x}|} \frac{\partial}{\partial t} \iint [p' n_i + \rho u_i(u_j - U_j) n_j] d\Sigma \right), \quad (2)$$

Solving Eq. (2) requires integrating over a surface Σ that encloses all sound sources. In the above, n_i is normal to the surface Σ, p' and ρ' are pressure and density fluctuations, ρ_0 is mean density, u_i is perturbation flow velocity and U_i is the velocity of the surface Σ. The source is at the origin, and $\mathbf{x}$ denotes the observer location. We choose a "porous" surface around the airfoil defined by one of the gridlines ($\xi = $ constant > 1; $\xi = 1$ is the airfoil surface) of the O-mesh around the airfoil. The FW-H solver has been validated previously against canonical problems (point monopole, dipole, and quadrupole) as well as against experimental data for aerodynamic noise from propellers [14].

3. Geometry modeling, meshing, and boundary conditions

The NACA 0012 airfoil is selected as the baseline airfoil. For the bioinspired airfoil, finlet fences are added near the airfoil trailing edge. The span length of the airfoil model in the simulations is 5.85% of the airfoil chord. A single-block, O-grid is used to generate a 2-D mesh around the baseline airfoil, which is repeated in the span direction to obtain the 3-D grid. The O-grid in the physical space (x, y, z) maps to an H-grid in the computational domain (ξ, η, ζ). The following orientation is used: $\widehat{\boldsymbol{e}}_\xi$ points radially out, $\widehat{\boldsymbol{e}}_\eta$ is in the circumferential direction, and $\widehat{\boldsymbol{e}}_\zeta$ is along the span direction such that the right-hand rule, $\widehat{\boldsymbol{e}}_\zeta = \widehat{\boldsymbol{e}}_\xi \times \widehat{\boldsymbol{e}}_\eta$, is obeyed. In the baseline grid used in this study, the distributions in the radial and circumferential directions of the O-mesh around the airfoil are similar to that described in Ref. [15], which was an LES of flow over an airfoil at $Re_c = 5 \times 10^5$. Based on the mesh sensitivity study performed in Ref. [15] and the recommendations from Georgiadis et al. [16], the grid spacing on the suction side was found to be appropriate for LES. In Ref. [15], only the suction side of the airfoil was resolved. To create the grid used in this study, the suction-side grid from Ref. [15] is mirrored on to the pressure side to resolve the flow over both surfaces of the airfoil.

Periodicity is imposed in the span direction ($\widehat{\boldsymbol{e}}_\zeta$). The periodic boundary conditions are implemented using the Overset grid approach in FDL3DI. A minimum of five-point overlap is required by FDL3DI to ensure high-order accurate interpolation between individual meshes. The airfoil surface is modeled as a no-slip, adiabatic wall. Freestream conditions are prescribed at the outer boundary and the grid is coarsened away from the airfoil surface in order for the filtering procedure to remove all perturbations from the flow before they reach the outer boundary. The computational time step, $\Delta\tau$ is chosen to be very small ($= 4 \times 10^{-5}$). Based on the study by Choi and Moin [17], in the turbulent flow region the computational time step in terms of wall units,

Table 1
Baseline grid metrics.

$N_\xi \times N_\eta \times N_\zeta$	y^+ avg, max	x^+ avg, max	z^+ avg, max
$410 \times 1937 \times 101$	0.567, 0.665	28.7, 37.1	14.9, 17.3

$\Delta t^+ = \Delta t u_\tau^2 / \nu \leq 0.048$, should be sufficiently accurate to resolve the near-wall turbulence. In the above, $\tau = tU_\infty/c$ is non-dimensional time ($\tau = 1$ is the time it takes for the flow to go past the airfoil), where c is the airfoil chord, t is the dimensional time, and U_∞ is the freestream flow speed.

3.1. Baseline airfoil mesh

The baseline is the NACA 0012 airfoil with a rounded trailing edge. The simulations are carried out at the chord-based Reynolds number, $Re_c = 5 \times 10^5$, the angle of attack, $\alpha = 0°$, and the flow Mach number, $M_\infty = 0.2$. The choice of the first cell height with these flow conditions gives an average y^+ of 0.567 for the baseline geometry. The turbulent boundary layer is highly resolved. As an example, the boundary layer at $x/c = 0.85$ contains 110 grid points with approximately 15 points in the viscous sublayer. The max grid stretching ratio at the top of the boundary layer is 1.04. Fig. 3 shows close-up, cross-sectional views of the O-grid around the baseline airfoil. For clarity, every third point in the radial and circumferential direction is shown in Fig. 3. Table 1 provides the grid metrics averaged over the turbulent flow region of the baseline simulation. The metrics are also averaged along the span.

3.2. Finlet fence geometry and mesh

The meshes for the one-step and stair-step fence simulations are obtained from the baseline mesh by performing hole-cutting (also called point-blanking). Hole-cutting involves removing mesh points that lie inside a solid. In the simulations presented in this work, the regions occupied by the fences (defined by specifying ranges $\xi_1 - \xi_2, \eta_1 - \eta_2$, and $\zeta_1 - \zeta_2$) are cut out as holes from the baseline grid and the no-slip condition is applied to the new boundaries thus created. The PEGASUS software [18] is used to perform hole-cutting.

Fig. 4 shows cross-sectional views of the single-step and stair-step finlet fence meshes; the views are zoomed in on the fence region to clearly show the geometric differences. The mesh points in the grey regions between the blue lines and the airfoil surface are marked as holes and removed from the calculation. Fig. 5 shows top views of the baseline mesh and the single-step fence mesh. The blue lines are the no-slip boundaries. The stair-step mesh is modeled in the same way except for the height of the fence which is varied in discrete steps with distance along the chord. The fence meshes were not further refined in the direction normal to the fence walls as the maximum z^+ with the baseline mesh is approximately 30.6 (located at the fence leading edge at the maximum height), which is not significantly greater than the span-averaged baseline z^+ value near the airfoil surface. Furthermore, we are not interested in precisely resolving the boundary layer on the surfaces of the fences. The working hypothesis is that the noise is reduced due to the displacement of energy-containing turbulence eddies away from the trailing edge, which can be captured even if the fence surfaces are modeled as inviscid walls. By not resolving the boundary layer on the sides of the fence walls, the near-fence-wall boundary layer flow physics may not be accurately captured. However, we believe that this level of resolution is not necessary to capture the observed noise reduction.
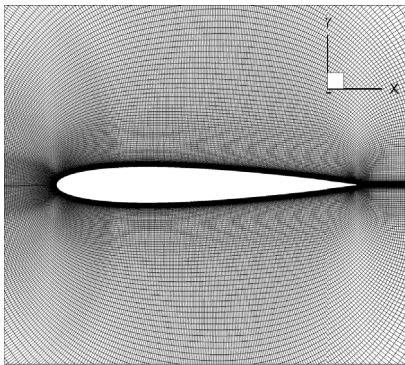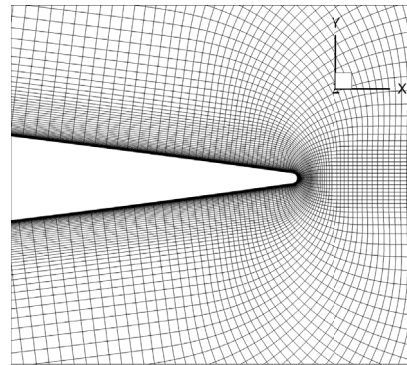
(a) Baseline mesh   (b) Baseline mesh near the TE

Fig. 3. The O-grid topology used in the simulations; shown here for the baseline airfoil. The trailing edge is rounded and the mesh near the TE ($0.90 \leq x/c \leq 1.04$) is shown in (b). Every third point along each axis is shown for clarity.
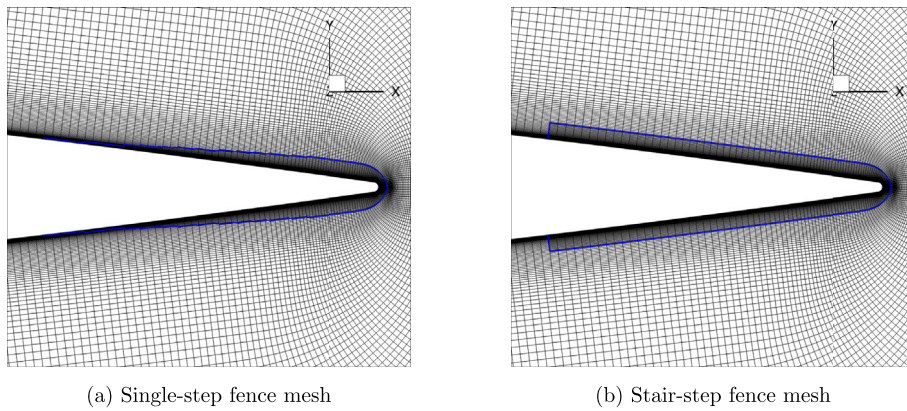
(a) Single-step fence mesh

(b) Stair-step fence mesh

Fig. 4. Cross-sectional (zoom) views ($0.861 \leq x/c \leq 1.005$) of the computational meshes used to simulate the single-step and stair-step fence geometries. Every other grid point along each axis is shown for clarity.
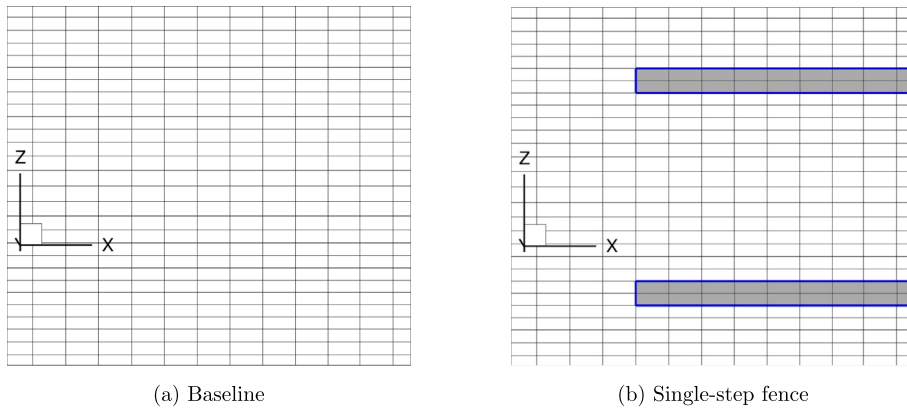

(a) Baseline

(b) Single-step fence

Fig. 5. Top views ($0.865 \leq x/c \leq 0.885$) of the baseline and single-step fence meshes. Each fence element is modeled to be two cells thick in the simulations.

A 3-D mesh containing a single fence element is created and then repeated six times along the span to obtain the full 3-D mesh with a span of 5.85% chord. The dimensions (height and spacing) of the two finlet fence geometries simulated are similar to configuration $F3$ in the experiments of Ref. [7], with the exception of the LE shape. The leading edge of the fence is at $x/c = 0.872$. The stair-step fence reaches the max height (H) at $x/c = 0.97$, where the height of the fence is about 19% of the boundary layer thickness ($y^+ \sim 110$). The x/c positions of the fence leading edge and maximum height are the same as in the experiment. The pitch of the fences is $1.5 \times H$ and the thickness is $0.17 \times H$. It should be emphasized that other than the holes (point blanking) introduced in the fence meshes, the grids for all three cases (baseline and two fences) are identical. This eliminates grid-to-grid differences in the simulation results when comparing the different designs.

3.3. Boundary layer trip

Since the simulation Re_c ($= 5 \times 10^5$) is smaller than that of the experiments ($\approx 2 \times 10^6$), the boundary layer on the airfoil surface is numerically tripped in the simulations. It should be noted that the boundary layer was also tripped in the experiments using a serrated tape. In the simulations, boundary layer tripping is achieved by placing a geometry-resolved "trip wire" at $x/c = 0.05$, measured from the leading edge of the airfoil. The trip wire is a square cylinder that extends throughout the span and is defined by blanking out cells in the regions occupied by the wire (see Fig. 6). The dimensions of the wire are defined by specifying ranges of the grid indices in the ξ, η and ζ directions; no-slip wall boundary condition is applied to the boundaries of the trip wire.

Fig. 7 shows the iso-surfaces of the Q-criterion ($Q = 10$) on the suction surface of the baseline airfoil for the tripped simulation. The trip wire successfully forces the boundary layer to transition well upstream, compared to where it transitions naturally, thereby achieving a turbulent boundary layer similar to what would occur via natural transition at high Re_c.
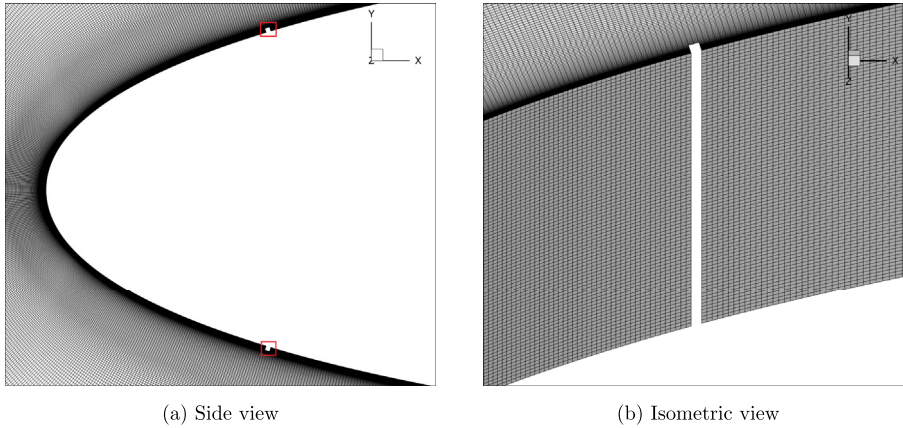
(a) Side view (b) Isometric view

Fig. 6. Mesh points that are blanked out to simulate the boundary layer trip wires (locations indicated with red squares in (a)). The nodes adjacent to the blanked-out points are assigned the no-slip wall boundary condition. The trip is applied across the entire length of the airfoil. (For interpretation of the references to colour in this figure legend, the reader is referred to the Web version of this article.)
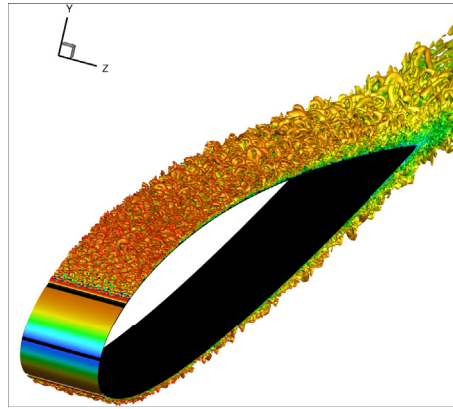

Fig. 7. Iso-surfaces of the Q-criterion ($Q = 10$) of forced boundary layer transition from the geometry-resolved trip wire.

3.4. Removal of transients

Several techniques are employed to reduce the computational cost of the simulations. Each simulation is initiated in 2-D, with a potential flow solution as the initial condition. The Navier-Stokes equations are then solved for the 2-D problem until statistical convergence is achieved; this typically takes about 10τ, where $\tau (= c/U_\infty)$ is the characteristic flow time. The solution is then replicated in the span direction to obtain an initial 3-D solution for the baseline geometry. Transients in the 3-D simulation are then removed, which takes between 3τ to 5τ. For the 3-D simulations with fences, the solution is obtained in two steps. First the 2-D solution is replicated over a single-fence span width and simulated with the fences modeled in the computation, and the solution is allowed to reach a statistically stationary state ($\approx 10\tau$). This solution is then repeated for as many fences as required ($= 6$ here) to fit in the 5.85% span length of the full 3-D geometry simulated. Transients are then removed in the full 3-D simulation (with the array of fences) by simulating the flow for another 5τ, before collecting data for noise analysis. Several methods are used to ensure the removal of transients. Each simulation is run until the integrated drag and lift forces become statistically stationary as well as the surface pressure spectra in the turbulent boundary layer is converged.

4. Results

This section presents the baseline validation and aeroacoustics results of the numerical simulations followed by a discussion on the noise reduction mechanisms with the fence finlet designs.
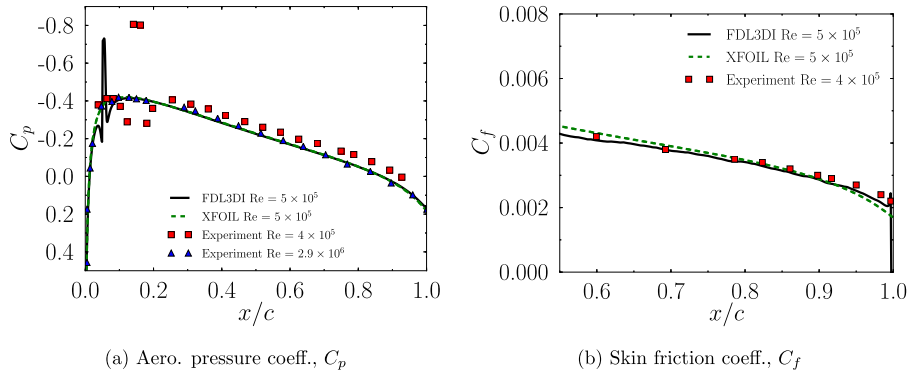
(a) Aero. pressure coeff., C_p (b) Skin friction coeff., C_f

Fig. 8. Time- and span-averaged C_p and C_f distributions from FDL3DI predictions ($Re_c = 5 \times 10^5$) compared with experiments ($Re_c = 4 \times 10^5$ and 2.9×10^6) and XFOIL simulations ($Re_c = 5 \times 10^5$).
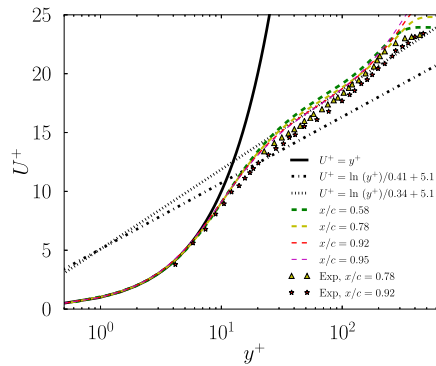

Fig. 9. Baseline mean velocity profiles normalized by friction velocity plotted in wall units at different chord locations. Measurements are from Lee and Kang [22].

4.1. Baseline validation

Once the transients are removed from the 3-D simulations, the simulation data is averaged in time for approximately 2.5τ with 63,000 samples to predict the aerodynamic performance. Fig. 8 (a) compares the predicted time- and span-averaged aerodynamic pressure coefficient (C_p) distributions of the baseline airfoil with experimental data and with XFOIL [19] predictions. The experimental measurements are for the NACA 0012 airfoil at $AOA = 0°$ from Sagrado et al. [20] and Gregory et al. [21] at Re_c of 4×10^5 and 2.9×10^6, respectively. The boundary layer is tripped on both surfaces of the airfoil. The trip is located at $x/c = 0.127$ in Sagrado et al. [20] and at $x/c = 0.05$ in Gregory et al. [21]. XFOIL results are also obtained with the boundary layer tripped at $x/c = 0.05$ and $Re_c = 5 \times 10^5$, which are the same conditions as in the FDL3DI simulation. The FDL3DI-predicted C_p agrees very well with the measured data over the entire airfoil except at the trip wire location where a spike is observed in the FDL3DI result. The agreement is better with the higher Re_c measurements. XFOIL does remarkably well in predicting the C_p distribution.

Fig. 8 (b) compares the FDL3DI-predicted skin friction coefficient (C_f) distribution over the airfoil surface with the measured data from Sagrado et al. [20] and XFOIL, where excellent agreement is seen with both the measured data and XFOIL.

Fig. 9 compares the baseline span-averaged normalized velocity profile, U^+, for different chord locations on the upper side of the airfoil from $x/c = 0.58$ to $x/c = 0.95$. The viscous sublayer is well resolved. The slope in the log-law region is found to be 1/0.34. While this value is slightly larger than the von Kármán constant ($= 1/0.41$), it is consistent with the measurements of Lee and Kang [22] of a turbulent flow over the NACA 0012 airfoil at $Re_c = 600,000$.

Fig. 10 compares the normalized Reynolds stresses for the baseline airfoil as computed using a) the current FDL3DI simulations, b) the DNS of a turbulent boundary layer with an adverse pressure gradient by Spalart and Watmuff [23], and c) the LES of the NACA 0012 at $Re = 4 \times 10^5$ and $\alpha = 0°$ by Wolf and Lele [24]. In the DNS, the Reynolds number based on the x-coordinate in the flow direction is $Re_x = 3.4 \times 10^5$. The pressure gradient parameter ($\beta = (\delta^*/\tau_w)dp/dx$), varies from 0 to 2 in the x direction, where the Reynolds stresses are at an x location corresponding to $\beta = 1$. The data from Ref. [24] and the current LES has a $\beta \approx 1$ at $x/c = 0.85$. Aside from the $\overline{u_1 u_1}$ peak near the wall in the DNS, good agreement is seen with the DNS results of Ref. [23] and with the LES results of Ref. [24].
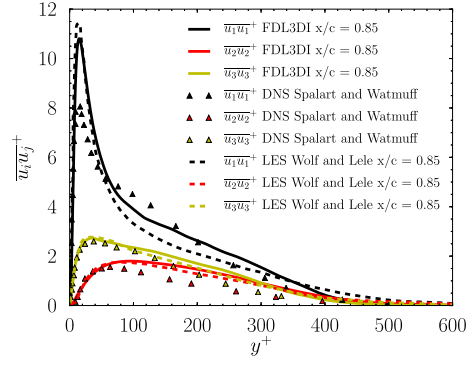
Fig. 10. Comparison of FDL3DI predictions of normalized Reynolds stresses for the baseline airfoil with DNS results of a turbulent boundary layer in an adverse pressure gradient from Spalart and Watmuff [23], and an LES of a NACA 0012 at $Re = 4 \times 10^5, \alpha = 0°$ from Wolf and Lele [24].
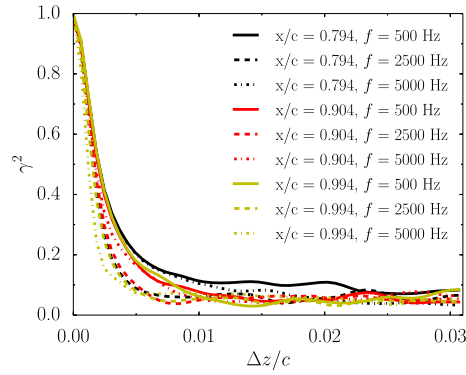

Fig. 11. Spanwise coherence squared (γ^2) on the upper surface of the baseline airfoil at $x/c = 0.794, 904,$ and 0.994 for $f = 500, 2500,$ and 5000 Hz.

Coherence squared, γ^2, between two points **x** and **y** is defined as

$$\gamma_{xy}^2(\omega) = \frac{|S_{xy}(\omega)|^2}{S_{xx}(\omega)S_{yy}(\omega)}, \tag{3}$$

where $S_{xx}(\omega)$ is pressure spectral density, $S_{pp}(\omega)$ evaluated at point **x** and $S_{yy}(w)$ is $S_{pp}(\omega)$ evaluated at point **y**. For spanwise coherence, points **x** and **y** are at a given chordwise location (x/c) but separated in the span direction such that $\mathbf{y} = \mathbf{x} + \Delta z\, \widehat{e}_k$, where $\widehat{e}_k$ is a unit vector along the span direction. The reference location to compute spanwise coherence is varied along the span. Each grid point is selected as a reference to compute one instance of coherence. All the instances of coherence so computed (101 in total) are then averaged to obtain the γ^2 reported here.

Spanwise coherence is typically used to assess if a simulated span in an LES is sufficient for all sources of sound to radiate independently. For the baseline simulation, $\gamma_{xy}^2(\omega)$ is computed using Eq. (3) and the Welch method [25] with 2000 samples of data ($\approx 7\tau$) divided into 20 segments with a 50% overlap. The Hanning window is applied over each segment. Zero padding is not used in computing Fourier Transforms. Fig. 11 plots the $\gamma^2(\omega)$ evaluated at three frequencies and at three x/c locations along the airfoil. The spanwise coherence decays to near zero suggesting that the span in the simulations is sufficient.

4.2. Surface pressure spectra

The primary noise generation mechanism in this low Mach number flow is the scattering into radiating sound of the hydrodynamic energy in the boundary layer turbulence by the airfoil trailing edge. Unsteady surface pressure near the trailing edge is therefore a measure of noise source strength. Surface pressure spectra are computed at $x/c = 0.975$. Numerical data is collected for approximately 5τ. Welch averaging is used with 1400 samples divided into 20 segments to reduce the scatter in the spectra. The spectra are also averaged over the span. The points that lie within the fences (marked as holes in the FDL3DI simulations) are removed in the averaging procedure.
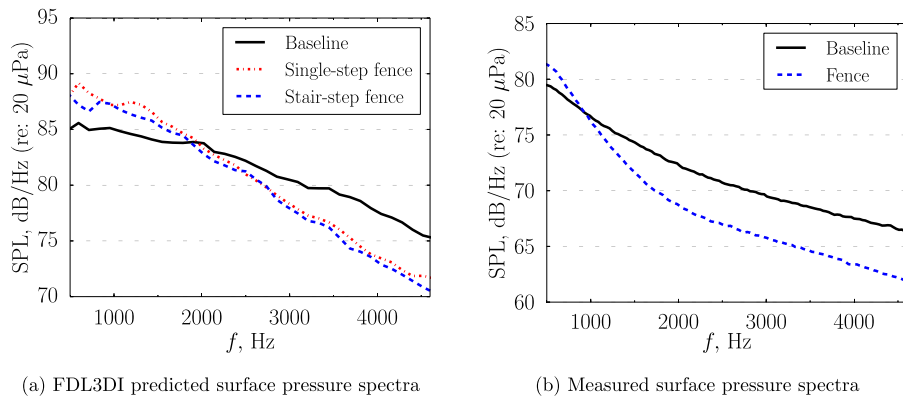
(a) FDL3DI predicted surface pressure spectra   (b) Measured surface pressure spectra

Fig. 12. Qualitative comparison between the predicted and measured surface pressure spectra at the trailing edge $x/c = 0.975$. Measurements are from Ref. [26].
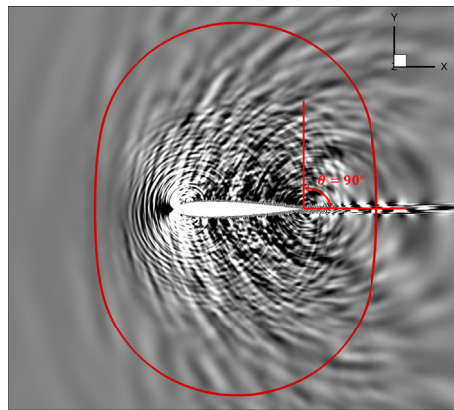

Fig. 13. Fluid dilatation contours for the baseline simulation. The FWH integration surface is marked with the red curve. Observer angle (θ) is measured from downstream. (For interpretation of the references to colour in this figure legend, the reader is referred to the Web version of this article.)

Fig. 12 (a) compares the predicted surface pressure spectra near the airfoil trailing edge from the three simulations - one baseline and two fence simulations. Compared to the baseline, a measurable reduction at high frequencies and an increase at low frequencies are observed in the predicted surface pressure spectra with both the single-step and stair-step fence geometry. These observations are compared *qualitatively* with measured surface pressure spectra from Ref. [26] (Fig. 12 (b)). The figures show that the predictions agree qualitatively with the measurements – reduction is observed at high frequencies and an increase in spectral magnitude is observed at low frequencies. Interestingly, the surface pressure reductions near the airfoil trailing edge are found to be almost insensitive to the leading edge geometry of the fence.

4.3. Far field aeroacoustics

Fluid dilatation ($\nabla.\boldsymbol{v}$) is representative of instantaneous acoustic perturbations. Fig. 13 shows the dilatation field for the baseline simulation, where the broadband noise from the airfoil trailing edge can be seen. A clear tonal noise signature is visible in the simulation, which emanates from the trip wire located on the airfoil surface at $x/c = 0.05$. The tonal noise from the trip wire is present in all three simulations. Vorticity contours near the trip wire are shown in Fig. 14. The contour plot shows the flapping shear layer downstream of the trip wire that causes the extraneous noise. While this noise source is undesirable in the simulations, the frequency of this tone is much higher than the broadband noise frequencies of interest. In a linearized acoustics sense, the effect of this extraneous tone on the relevant broadband noise spectrum is ignored in the current predictions.

The in-house FW-H solver is used to calculate the far field noise. For the baseline airfoil, the integration (Kirchoff) surface can be selected as the airfoil surface. However, for the fence geometries, the FW-H surface has to include the walls of each fence to ensure that noise contributions from all surfaces are included. Sampling data on the fence surfaces is quite tedious as they cannot be defined as constant ξ, η, or ζ boundaries. A permeable surface is therefore selected that encloses the fences and the airfoil. Furthermore, the location of the permeable FW-H surface (marked with the red curve in Fig. 13) is chosen so that it is outside the undesired, high-frequency waves emanating from the trip wire. The integration surface extends from $-0.6 < x/c < 1.6$
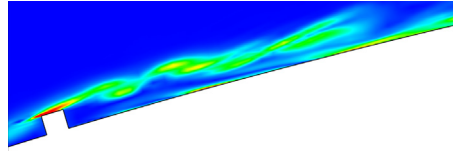
Fig. 14. The shear layer behind the trip wire visualized using contours of vorticity magnitude.

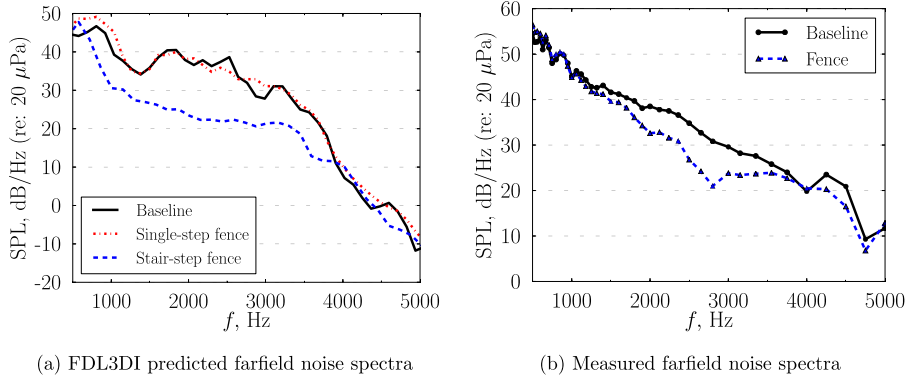(a) FDL3DI predicted farfield noise spectra

(b) Measured farfield noise spectra

Fig. 15. Qualitative comparison between the FDL3DI predicted and measured farfield noise spectra at an observer located at $\theta = 90°$.

and $-0.5 < y/c < 0.5$. Although the surface is not close to the airfoil, the grid is stretched very slowly up to the integration surface (stretching ratio <1.06 near the FW-H surface). Therefore, the amount of numerical dissipation in the frequencies of interest is expected to be small.

Fig. 15 shows the predicted far field noise for the baseline and the two fences at polar angle, $\theta = 90°$. The polar angle is measured from downstream and is positive in the counter-clockwise direction (see Fig. 13). The Power Spectral Density (PSD) is computed using the Welch method with 1200 samples ($\approx 4\tau$) divided into 13 segments and a 50% overlap between segments. Commensurate with the observed reductions in surface pressure spectra, the stair-step fence yields a substantial reduction in the farfield noise compared to the baseline between 500 Hz–5 kHz. However, despite similar reductions in surface pressure spectra near the airfoil trailing edge with the single-step fence, no reduction is observed in the far field noise in the single-step simulation.

To investigate why the single-step fence does not yield farfield noise reduction, normalized unsteady surface pressure ($C_{p,rms}$) is investigated at $x/c = 0.87$, which is immediately upstream of the fence leading edge location. Fig. 16 shows contours of $C_{p,rms}$ for the baseline, single-step, and stair-step fence simulations on a cross-stream plane at $x/c = 0.87$. Fig. 17 quantitatively compares the span-averaged surface pressure spectra between the three geometries at $x/c = 0.87$. The single-step fence clearly has much higher unsteady surface pressure near the fence leading edge than the stair-step fence or the baseline airfoil. Contrasting this with the spectra comparisons near the airfoil trailing edge (see Fig. 12), we note that while the single-step fence geometry successfully reduces the unsteady surface pressure near the airfoil trailing edge, it actually increases the unsteady pressure near
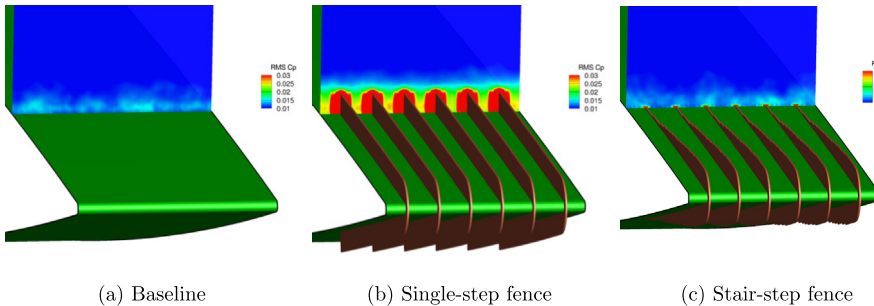

(a) Baseline

(b) Single-step fence

(c) Stair-step fence

Fig. 16. Contours of $C_{p,rms}$ on a cross-stream plane immediately upstream of the fence leading edge ($x/c = 0.87$).
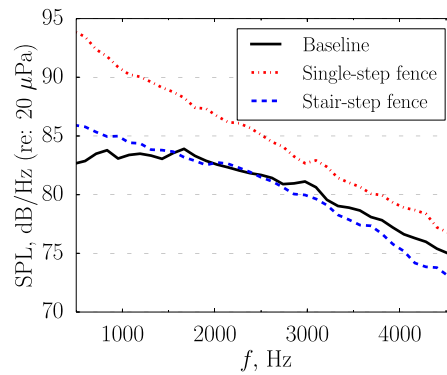
Fig. 17. Comparison of unsteady surface pressure spectra at $x/c = 0.87$ between the baseline, single-step fence, and stair-step fence. The spectra has been averaged over the span.

the leading edge of the fences. We hypothesize that this unsteady pressure acts as localized lift on the leading edges of the fences in the single-step fence geometry and radiates as sound. This additional noise source offsets the benefit of reduced airfoil trailing edge noise due to the observed reduction in unsteady surface pressure there.

The predicted results for the stair-step fence geometry can be compared qualitatively with the measured farfield noise spectrum from Ref. [26] shown in Fig. 15 (b). The measured farfield noise was obtained using beamforming and integrating the one-twelfth octave band spectra over a two-dimensional area near the trailing edge. Although the difference in span lengths between the simulation and experiment is accounted for using Kato's correction [27], due to the difference in the baseline airfoil used between the simulations and the experiment, the SPL of the predicted and measured noise cannot be quantitatively compared. However, the predicted noise-reduction trends are consistent with the measurements. Little to no noise reduction is observed above 4 kHz and a noise reduction of up to 10 dB is observed between 1 kHz and 4 kHz. Clark et al. [26] have suggested that the low frequencies (below 1 kHz) may have a facility noise contribution and hence any potential reduction in noise due to finlets at those frequencies will not be captured by the measurements. This may explain the differences in noise reduction with the finlets for frequencies below 1 kHz.

4.4. Noise reduction mechanisms

Two hypotheses are put forth to explain the observed farfield noise reduction with the fence finlets: (1) the fences lift the turbulence eddies away from the scattering (airfoil trailing) edge, and (2) the fences reduce the spanwise correlation length. These hypotheses are investigated using the simulation results in this section.

4.4.1. Turbulence kinetic energy

To assess the first hypothesis, normalized turbulence kinetic energy (TKE) is obtained by averaging over 2.5τ. The TKE does not significantly change if more than 2.5τ of data is used for the averaging process. Contour plots of normalized TKE are compared between the baseline and the two fence simulations on cross-stream planes at two chordwise locations in Figs. 18 and 19. The plots show isometric views with the cross-stream cut planes. At $x/c = 0.85$, which is upstream of the fences, the TKE is concentrated in the boundary layer close to the airfoil surface in all three simulations (see Fig. 18). However, at the airfoil trailing edge, the TKE close to the airfoil surface (trailing edge) is substantially reduced with the fences, and appears to be con-
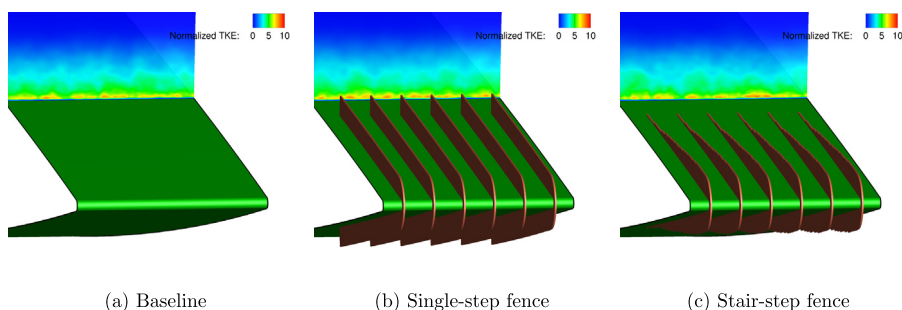

(a) Baseline   (b) Single-step fence   (c) Stair-step fence

Fig. 18. Normalized turbulent kinetic energy (k/u_τ^2) contours for the baseline, single-step fence, and stair-step fence simulations at $x/c = 0.85$ (upstream of the fence).
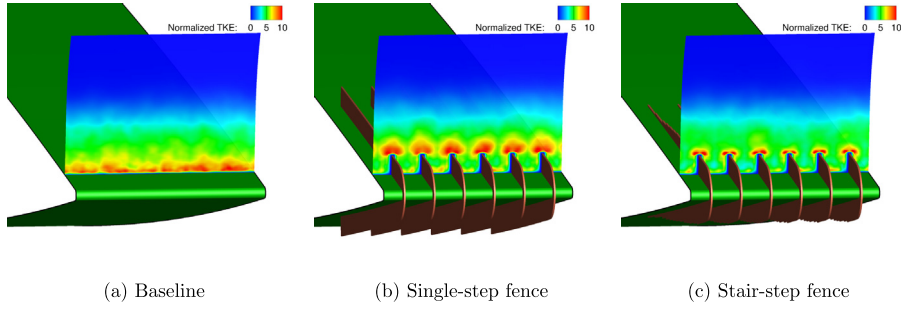
(a) Baseline   (b) Single-step fence   (c) Stair-step fence

Fig. 19. Normalized turbulent kinetic energy (k/u_τ^2) contours for the baseline, single-step fence, and stair-step fence simulations at $x/c = 0.975$ near the airfoil trailing edge.
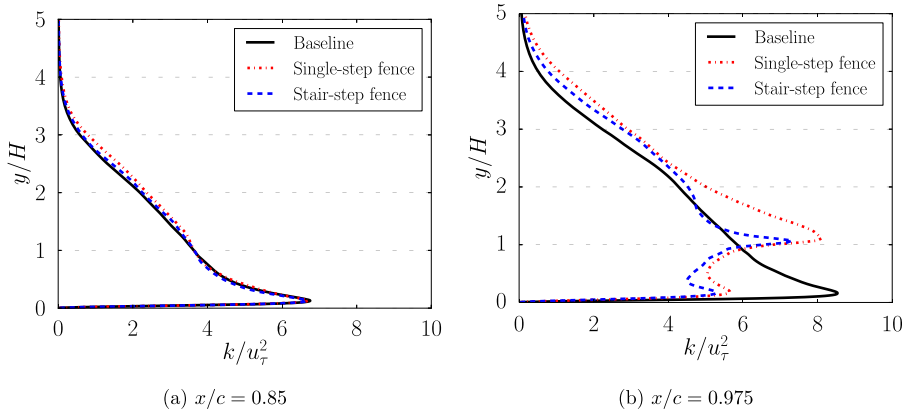

(a) $x/c = 0.85$ (b) $x/c = 0.975$

Fig. 20. Span-averaged normalized turbulent kinetic energy (k/u_τ^2) profiles compared between the baseline and fence simulations: (a) upstream of the fence at $x/c = 0.85$, and (b) near the airfoil trailing edge at $x/c = 0.975$.

centrated above the fences (see Fig. 19). Fig. 19 clearly shows that the separation distance between the source (unsteadiness in the turbulence) and the scattering airfoil trailing edge is increased. Afshari et al. [28] conducted an experiment with a similar finlet fence geometry installed over a flat plate at zero incidence. They observed similar trends as seen in the current predictions for turbulence intensity (TI); with the fences, the TI decreased near the flat plate and increased above the fences.

Fig. 20 compares the span-averaged TKE profiles between the baseline and the fence geometries at the two cross-stream locations corresponding to the plots in Figs. 18 and 19. The line plots quantitatively show the reduction in TKE near the surface and concentration of TKE above both the single-step and stair-step fences. Note that the ordinate in Fig. 20 is normalized by the maximum fence height, H. These results substantiate the first hypothesis for the observed reduction in unsteady surface pressure and the farfield noise with the fence finlets. While the TKE redistribution to the top of the fences also occurs with the single-step fence, the overall farfield noise is not reduced due to the additional noise source at the fence leading edge, as discussed earlier.

4.4.2. Spanwise coherence

Amiet [29] provides an analytical expression for the farfield pressure PSD, $S_{pp}(\omega)$ of the sound radiated from a turbulent flow past the trailing edge of a half-plane. Per Amiet [29], $S_{pp}(\omega) \propto l_y(\omega)S_{qq}(\omega)$, where ω is the angular frequency, $S_{qq}(\omega)$ is the surface pressure PSD, and $l_y(\omega)$ is the spanwise correlation length of the pressure fluctuations. A reduction in spanwise coherence ($\gamma_{xy}^2(\omega)$), which is a measure of $l_y(\omega)$, can reduce the farfield noise even if the surface pressure PSD remains unchanged.

The procedure described in Section 3.1 is followed and Eq. (3) is used to compute $\gamma_{xy}^2(\omega)$ for the baseline and stair-step fence simulations. A total of 7.34τ of data, consisting of 2039 samples divided into 30 segments for spectral averaging is used for the calculations. Fig. 21 compares γ^2 of the unsteady surface pressure near the trailing edge ($x/c = 0.97$) as a function of the spanwise separation distance ($\Delta z/c$) for the baseline and stair-step fence simulations. Coherence plots are drawn for two example frequencies to highlight the characteristics in the low- and high-frequency regions. The vertical dashed lines in the plots represent the spanwise location of the fences. The fences are equidistant and the fence pitch (distance between adjacent fence walls) is P.
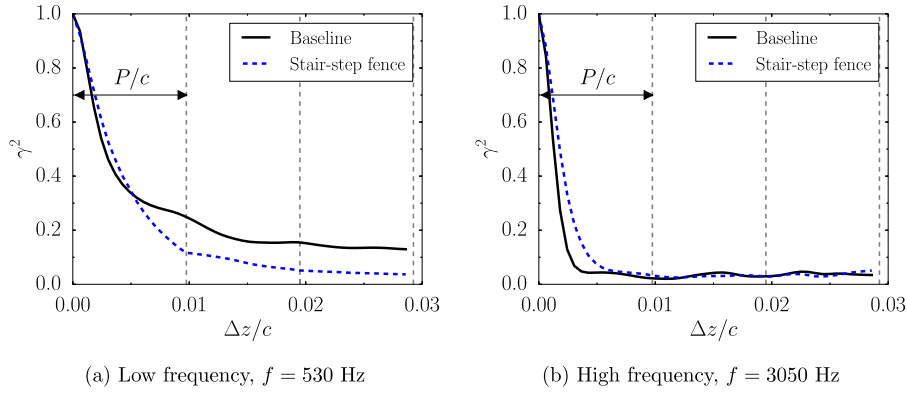
Fig. 21. Spanwise coherence, $\gamma^2(\omega)$ of unsteady surface pressure at the trailing edge $x/c = 0.97$ for a) low, and b) high frequencies.
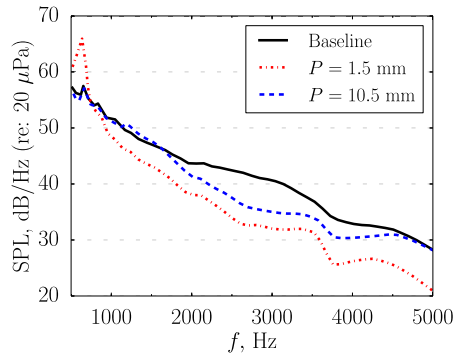

Fig. 22. Measured farfield noise spectra from Clark et al. [7] showing the effect of fence spacing. For all cases, the maximum height of the fences, $H = 4$ mm.

For separation distances greater than the fence pitch, i.e., $\Delta z > P$, we note that the fences reduce γ^2 at low frequencies (Fig. 21 (a)). At high frequencies, the coherence is already small for $\Delta z > P$ and the fences do not reduce it any further (Fig. 21 (b)). The simulation results show a farfield noise reduction at low frequencies with the stair-step fence despite an increase in the unsteady surface pressure PSD (see Figs. 12 (a) and 15). This analysis suggests that the reduction in spanwise coherence is responsible for the reduction in farfield noise at low frequencies.

This argument is supported by the following observation of the measurements by Clark [7]. Low-frequency noise reduction was observed in the experiments when the fence pitch was reduced (see Fig. 22). Since fences reduce γ^2 for spanwise distances greater than the fence pitch, a tighter pitch implies a reduction in span correlation length, and consequently a reduction in farfield noise.

5. Conclusions

This paper presents numerical investigations of airfoil geometries inspired by the down coat of the owl. The canopy effect of the down coat is achieved using the finlet fences proposed by Clark et al. [6]. Large eddy simulations are performed for the baseline (NACA 0012) airfoil and two airfoils with the finlet fences. The baseline simulation results are validated against measured data available in the literature for aerodynamic pressure coefficient (C_p) and boundary layer profiles, and against previous DNS and LES results for Reynolds stresses. Qualitative comparisons are drawn with experiments with the fences to verify the trend prediction ability of the approach. The following conclusions are drawn from the study.

1. Comparisons of surface pressure spectra show a reduction at high frequencies and a slight increase in the low frequencies near the airfoil trailing edge with the fences.
2. Farfield noise spectra comparisons show reductions of up to 10 dB at frequencies ranging from 500 to 5000 Hz for the stair-step fence simulation; no reductions are observed for the single-step fence simulation.
3. Contour plots and span-averaged profiles of normalized turbulence kinetic energy (TKE) show a clear redistribution of TKE away from the airfoil trailing edge.
4. A comparison of the spanwise coherence of the unsteady surface pressure shows that the stair-step fence reduces γ^2 at low frequencies for normalized separation distances $\Delta z/c > P/c$.

The results show that one of the reasons for the observed noise reduction with the fences is the increased source-scattering edge separation distance, which makes the edge scattering process less efficient. Another mechanism of farfield noise reduction at low frequencies is identified to be a reduction in spanwise coherence. The lack of farfield noise reduction from the single-step fence demonstrates the importance of having the fence leading edge nearly aligned with the incoming flow.

Acknowledgments

References

[1] R.D. Sandberg, L.E. Jones, Direct numerical simulations of low Reynolds number flow over airfoils with trailing-edge serrations, J. Sound Vib. 330 (16) (2011) 3818–3831.
[2] M. Roger, C. Schram, L. De Santana, Reduction of airfoil turbulence-impingement noise by means of leading-edge serrations and/or porous material, in: 19th AIAA/CEAS Aeroacoustics Conference, American Institute of Aeronautics and Astronautics, 2013.
[3] B.R. Agrawal, A. Sharma, Numerical analysis of aerodynamic noise mitigation via leading edge serrations for a rod–airfoil configuration, Int. J. Aeroacoustics 15 (8) (2016) 734–756.
[4] J.W. Jaworski, N. Peake, Aerodynamic noise from a poroelastic edge with implications for the silent flight of owls, J. Fluid Mech. 723 (2013) 456–479.
[5] A.V. Cavalieri, W.R. Wolf, J. Jaworski, Acoustic scattering by finite poroelastic plates, in: 20th AIAA/CEAS Aeroacoustics Conference, AIAA Aviation, American Institute of Aeronautics and Astronautics, 2014.
[6] I.A. Clark, W. Devenport, J.W. Jaworski, C. Daly, N. Peake, S. Glegg, Noise generating and suppressing characteristics of bio-inspired rough surfaces, in: 20th AIAA/CEAS Aeroacoustics Meeting, American Institute of Aeronautics and Astronautics, 2014.
[7] I.A. Clark, N.W. Alexander, W. Devenport, S. Glegg, J.W. Jaworski, C. Daly, N. Peake, Bioinspired trailing-edge noise control, AIAA J. 55 (3) (2017) 740–754.
[8] R. Dougherty, Extensions of DAMAS and benefits and limitations of deconvolution in beamforming, in: 11th AIAA/CEAS Aeroacoustics Conference, 2005, p. 2961.
[9] A. Bodling, B.R. Agrawal, A. Sharma, I.A. Clark, N.W. Alexander, W. Devenport, Numerical investigations of bio-inspired blade designs to reduce broadband noise in aircraft engines and wind turbines, in: 55th AIAA Aerospace Sciences Meeting, American Institute of Aeronautics and Astronautics, 2017.
[10] A. Bodling, B.R. Agrawal, A. Sharma, I.A. Clark, N.W. Alexander, W. Devenport, Numerical investigation of bio-inspired blade designs at high Reynolds numbers for ultra-quiet aircraft and wind turbines, in: 23rd AIAA/CEAS Aeroacoustics Conference, American Institute of Aeronautics and Astronautics, 2017.
[11] R.M. Visbal, V.D. Gaitonde, On the use of higher-order finite-difference schemes on curvilinear and deforming meshes, J. Comput. Phys. 181 (1) (2002) 155–185.
[12] B.R. Agrawal, A. Sharma, Numerical investigations of bio-inspired blade designs to reduce broadband noise in aircraft engines and wind turbines, in: 2016 AIAA SciTech Meeting, American Institute of Aeronautics and Astronautics, 2016.
[13] J.E.F. Williams, D.L. Hawkings, Sound generation by turbulence and surfaces in arbitrary motion, Phil. Trans. Roy. Soc. Lond. Math. Phys. Sci. 264 (1151) (1969) 321–342.
[14] A. Sharma, H. Chen, Prediction of aerodynamic tonal noise from open rotors, J. Sound Vib. 332 (6).
[15] R.M. Visbal, Numerical exploration of flow control for delay of dynamic stall on a pitching airfoil, in: 32nd AIAA Applied Aerodynamics Conference, American Institute of Aeronautics and Astronautics, 2014.
[16] N.J. Georgiadis, D.P. Rizzetta, C. Fureby, Large-eddy simulation: current capabilities, recommended practices and future research, AIAA J. 48 (8) (2010) 1772–1784.
[17] H. Choi, P. Moin, Effects of the computational time step on numerical solutions of turbulent flow, J. Comput. Phys. 113 (1994) 1–4.
[18] E.N. Suhs, E.S. Rogers, E.W. Dietz, Pegasus 5: an automated pre-processor for overset-grid CFD, in: 32nd AIAA Fluid Dynamics Conference, American Institute of Aeronautics and Astronautics, 2002.
[19] M. Drela, Xfoil: an analysis and design system for low Reynolds number airfoils, in: Low Reynolds Number Aerodynamics, Springer, 1989, pp. 1–12.
[20] A.G. Sagrado, T. Hynes, Wall pressure sources near an airfoil trailing edge under turbulent boundary layers, J. Fluid Struct. 30 (2012) 3–34.
[21] N. Gregory, C.L. O'Reilly, Low-speed Aerodynamic Characteristics of Naca 0012 Aerofoil Section, Including the Effects of Upper-Surface Roughness Simulating Hoar Frost, Tech. Rep. NASA Reports and Memoranda 3726, 1970.
[22] H. Lee, S.H. Kang, Flow characteristics of transitional boundary layers on an airfoil in wakes, ASME J. Fluids Eng. 122 (2000) 522–532.
[23] P. Spalart, J.H. Watmuff, Experimental and numerical study of a turbulent boundary layer with pressure gradient, J. Fluid Mech. 249 (1993) 337–371.
[24] W.R. Wolf, S.K. Lele, Trailing edge noise predictions using compressible les and acoustic analogy, in: 17th AIAA/CEAS Aeroacoustics Conference, American Institute of Aeronautics and Astronautics, 2011.
[25] P. Welch, The use of fast fourier transform for the estimation of power spectra: a method based on time averaging over short, modified periodograms, IEEE Trans. Audio Electroacoust. 15 (2) (1967) 70–73.
[26] I.A. Clark, Bio-Inspired Control of Roughness and Trailing Edge Noise, PhD thesis, Virginia Polytechnic Institute and State University, 2017 (under review).
[27] C. Kato, M. Ikegawa, Large eddy simulation of unsteady turbulent wake of a circular cylinder using the finite element method, in: Advances in Numerical Simulation of Turbulent Flows, vol. 1, 1991, pp. 49–56.
[28] A. Afshari, M. Azarpeyvand, A.A. Dehghan, M. Szőke, Effects of streamwise surface treatments on trailing edge noise reduction, in: 23rd AIAA/CEAS Aeroacoustics Conference, American Institute of Aeronautics and Astronautics, 2017.
[29] R.K. Amiet, Noise due to turbulent flow past a trailing edge, J. Sound Vib. 47 (3) (1976) 387–393.